agronomy

MDPI

Article

Integrating CEDGAN and FCNN for Enhanced Evaluation and Prediction of Plant Growth Environments in Urban Green Spaces

Ying Wang [1,†], Zhansheng Mao [2,3,†], Hexian Jin [1,*], Abbas Shafi [4], Zhenyu Wang [2,3] and Dan Liu [2,3,*]

[1] College of Landscape Architecture, Zhejiang A&F University, Hangzhou 311300, China; 20040073@zafu.edu.cn
[2] State Key Laboratory of Subtropical Silviculture, Zhejiang A&F University, Lin'an 311300, China; maozhansheng@stu.zafu.edu.cn (Z.M.)
[3] Key Laboratory of Soil Contamination Bioremediation of Zhejiang Province, Zhejiang A&F University, Lin'an 311300, China
[4] Institute of Computer Sciences, The University of Agriculture Peshawar, Peshawar 25000, Khyber Pakhtunkhwa, Pakistan
* Correspondence: lotusjhx@zafu.edu.cn (H.J.); liudan@zafu.edu.cn (D.L.)
† These authors contributed equally to this work.

Abstract: Conducting precise evaluations and predictions of the environmental conditions for plant growth in green spaces is crucial for ensuring their health and sustainability. Yet, assessing the health of urban greenery and the plant growth environment represents a significant and complex challenge within the fields of urban planning and environmental management. This complexity arises from two main challenges: the limitations in acquiring high-density, high-precision data, and the difficulties traditional methods face in capturing and modeling the complex nonlinear relationships between environmental factors and plant growth. In light of the superior spatial interpolation capabilities of CEDGAN (conditional encoder–decoder generative adversarial neural network), notwithstanding its comparative lack of robustness across different subjects, and the excellent ability of FCNN (fully connected neural network) to fit multiple nonlinear equation models, we have developed two models based on these network structures. One model performs high-precision spatial attribute interpolation for urban green spaces, and the other predicts and evaluates the environmental conditions for plant growth within these areas. Our research has demonstrated that, following training with various samples, the CEDGAN network exhibits satisfactory performance in interpolating soil pH values, with an average pixel error below 0.03. This accuracy in predicting both spatial distribution and feature aspects improves with the increase in sample size and the number of controlled sampling points, offering an advanced method for high-precision spatial attribute interpolation in the planning and routine management of urban green spaces. Similarly, FCNN has shown commendable performance in predicting and evaluating plant growth environments, with prediction errors generally less than 0.1. Comparing different network structures, models with fewer hidden layers and nodes yielded superior training outcomes.

Keywords: neural networks; urban green space; predictive interpolation; complex nonlinear modeling

Citation: Wang, Y.; Mao, Z.; Jin, H.; Shafi, A.; Wang, Z.; Liu, D. Integrating CEDGAN and FCNN for Enhanced Evaluation and Prediction of Plant Growth Environments in Urban Green Spaces. *Agronomy* **2024**, *14*, 938. https://doi.org/10.3390/agronomy14050938

Academic Editor: Gniewko Niedbała

Received: 8 April 2024
Revised: 28 April 2024
Accepted: 29 April 2024
Published: 30 April 2024

1. Introduction

Urban green spaces are an essential component of urban ecosystems. Urban green spaces not only offer aesthetic and comfortable recreational facilities but also render multifaceted ecological functions such as climate regulation, air purification, soil conservation, and enhancement of biodiversity [1–4]. Accurate assessment and prediction of the environmental conditions for plant growth in green spaces is crucial for ensuring their health and sustainability. The environment significantly influences plant health in these areas [5]. Furthermore, since plants are the primary constituents of green spaces, they play a major role in determining the overall health and sustainability of these areas [6]. The attributes

and metrics of urban green spaces exhibit their quality and benefits, which has significantly influenced the planning, designing, and management of green spaces and urban areas [7]. The scientific monitoring and assessment of urban green space attributes has emerged as an integral aspect of urban ecological construction and sustainable development [8]. However, the environmental assessment of the health and plant growth of urban green spaces is an important but complex task in the field of urban planning and environmental management.

First, the inherent robust spatial heterogeneity of urban green spaces implies that attributes of green spaces can vary considerably across different locales in similar or proximate environmental conditions [8]. Constraints such as work volume and obtaining high-density and high-precision data on urban green spaces in practical scenarios become challenging [9]. We are often limited to represent the overall status of a region based on sparse sampling points.

This process requires high-precision interpolation and prediction of the gaps between these points to acquire comprehensive and continuous spatial distribution maps for the attributes of green spaces. This typically includes spatial interpolation using geospatial information technology and data acquisition through remote sensing techniques. Traditional interpolation methods, such as Kriging, inverse distance weighting, and spline interpolation, are based on statistical or mathematical models to estimate values at unknown points. These methods generally assume that soil indicators follow a certain deterministic or stochastic spatial distribution, and calculate interpolation weights based on the distance or similarity between sampling points [10]. Although these methods are simple and user-friendly, they have limitations, such as requiring data to meet the presuppositions of the interpolation method—ordinary Kriging, for instance, requires data variations to be normally distributed. They depend on the number and distribution of sampling points; when sampling points are sparse or uneven, the interpolation results are prone to bias or distortion. They cannot reflect the complex spatial variations in the soil indicators and only generate smooth or linear interpolation surfaces [11,12]. In recent years, with the advancement of remote sensing technology, particularly the widespread use of high-resolution and hyperspectral remote sensing data, the role of remote sensing in urban green space assessment has become increasingly significant [13–15]. Remote sensing allows researchers to quickly gather extensive data on urban green spaces, including vegetation cover, types of vegetation, and health status [16–18]. Using drones or satellite remote sensing data to analyze vegetation has become a common method [19–21]. Remote sensing provides wide-ranging, high-resolution, multi-temporal vegetation information for urban green spaces [17,22,23], offering effective data support for the monitoring and evaluation of urban green spaces. Additionally, combining remote sensing image processing techniques, such as image classification and vegetation index calculations [24,25], can further enhance the efficiency of data use and the accuracy of assessments.

Remote sensing observations serve as an efficient data collection method that can cover vast areas. However, the complexity of data processing and analysis, as well as the high level of expertise required, often limit its further application. For example, the Normalized Difference Vegetation Index (NDVI) is a widely used indicator of vegetation vigor that reflects the photosynthetic activity and biomass of vegetation. NDVI is calculated from the reflectance in the near-infrared and red light bands, with values ranging from -1 to 1. Generally, higher NDVI values indicate better vegetation growth. NDVI is known for its simplicity in calculation, direct reflection of conditions, and wide applicability [26].

However, using NDVI alone to assess the vegetation vigor of urban green spaces presents several issues and challenges, such as influences from atmospheric conditions, soil, and bodies of water, as well as the inability to distinguish between different types of vegetation [27,28]. Due to the diversity of vegetation types in urban green spaces, different types exhibit varying responses to NDVI at different times [29,30]. Consequently, the NDVI values and ranges used to determine whether vegetation is thriving also vary.

Research studies have initiated the integration of deep learning models into spatial data interpolation problems due to recent breakthroughs in deep learning across various

domains. Deep learning models are distinguished by their robust capability for high-dimensional, nonlinear function fitting and adaptive learning. This can autonomously extract features and patterns from vast data, enabling the modeling and prediction of complex data sets [31]. The Li has introduced a spatial interpolation method for soil temperature based on Long Short-Term Memory (LSTM) networks [32], harnessing LSTM's memory units and forget gates to grasp the dynamic temporal and spatial variations of soil temperature [33]. The attentive graph neural network (GNN) has been employed for the unsupervised spatial interpolation of air quality [34]. This approach adopts an encoder–decoder paradigm, where the encoder and decoder learn independently through distinct processes. The encoder learns a set of functions that generate spatial embedding by aggregating features from surrounding areas. The decoder, on the other hand, utilizes gated recurrent units and fully connected layers to estimate air quality index at the target location [35].

The local connectivity and shared weight of the CNN [36] architecture, relative to traditional methods, allow the model to focus on features close to each other as well as features far apart. This coincides with the goal of numerous spatial interpolation analyses, which allow the model to consider the effects of both neighboring and far-away samples on interpolation [37]. For example, a study has proposed a digital soil mapping (DSM) method based on convolutional neural networks (CNNs). This study has predicted soil carbon content at several depths across the country after training the CNN model accordingly using Chile as the study area. The CNN model has reduced the error by 30% as compared to CNN prediction results with conventional techniques [38].

These methods have emphasized the effectiveness and superiority of deep learning models for spatial data interpolation. But conventional singular deep learning techniques have been deficient in precision. For instance, they typically rely on supervised learning, necessitating vast labeled data for model training [39,40]. In practical applications, the labeled data are often scarce and costly [41]. Traditional deep learning models, primarily pixel-based or point-based, require spatial data to be transformed into pixel or point format, leading to information loss and increased computational overhead [42].

A study by Zhu [43] integrated convolutional neural networks, encoders, decoders, and conditional generative adversarial networks to create the conditional encoder–decoder generative adversarial neural network (CEDGAN) for spatial interpolation, addressing the issues mentioned above. Traditional CGANs primarily focus on feature labels, and the auxiliary information input into the model typically lacks spatial coupling information. This is mainly to generate fake images of specific categories that are indistinguishable by discriminators. However, spatial interpolation requires accurate spatial prediction and estimation, not merely generating data that discriminators cannot recognize [44]. The CEDGAN model combines the encoder–decoder structure with traditional adversarial learning principles. Compared to conventional CGANs, it can learn deep features of spatial data from the training set and their complex interactions with local structural patterns, producing interpolation results that closely resemble real data.

This model, when employed for DEM data interpolation and prediction, exhibited superior performance, by achieving interpolation precision surpassing traditional methods even under low data requirements. The CEDGAN network learns underlying spatial structural features of data, which can be extrapolated to other domains with varied distributions. However, when applied to data vastly different from the training set, its significantly deteriorates prediction efficacy.

Secondly, the inherent complexity of urban environments poses additional challenges to assessing the health of urban green spaces and the quality of their plant growth environments. Compared to natural environments, urban green spaces are influenced by a greater number of—and more complex—factors [45–47]. When addressing the complex system of urban green spaces, traditional evaluation and prediction methods exhibit some clear limitations. These include a limited capacity to process complexity, with traditional approaches struggling to capture and model the intricate nonlinear relationships between

environmental factors and their impact on plant growth [48]. The capacity for dynamic prediction is also lacking; traditional methods typically focus on static analysis and struggle to predict the real-time effects of environmental changes on plant growth [49]. Fully connected neural networks (FCNNs), as an advanced deep learning technology, offer a novel methodology for the evaluation and prediction of the urban green space plant growth environment. The core advantage of FCNNs lies in their exceptional feature learning capability, which allows them to automatically discover and utilize complex, nonlinear relationships within environmental data without the need for pre-assumed forms of data interaction [50–52]. This capability is particularly suited for addressing the multivariate, high-dimensional challenges inherent in urban green space environmental evaluations, including, but not limited to, the combined effects of soil quality, climate change, and human interventions.

Furthermore, FCNNs are capable of integrating and analyzing a vast array of data from different sources, such as satellite remote sensing data, ground monitoring station data, and socio-economic data, providing a comprehensive evaluation framework [53,54]. This not only enhances the precision of evaluations but also significantly boosts the model's capacity to handle complex systems. Moreover, FCNNs support the input of real-time data, enabling the model to dynamically predict changes in the plant growth environment. This offers immediate, accurate decision support for urban green space management.

In light of the superior spatial interpolation capabilities of CEDGAN, notwithstanding its relatively poor robustness, and given the FCNN's exceptional ability to fit multiple nonlinear equation models, this study proposes to retrain a predictive model based on the CEDGAN network structure to explore its feasibility for the high-precision interpolation of urban green space spatial attributes. Models trained using CEDGAN will be able to provide more high-precision spatial distribution data for future models with the same resource investment. Concurrently, leveraging the spatial attributes of green spaces, a model for predicting the environmental conditions conducive to plant growth in urban green areas will be trained using the FCNN network. Models trained on FCNNs will be able to offer excellent methods for fitting multiple nonlinear relationships, which will help enhance the accuracy of future models.

Specifically, in this study, we first utilize the excellent spatial interpolation capabilities of CEDGAN to perform high-precision spatial interpolation on sparse data; then, we input the high-precision remote sensing data corresponding to spatial locations and the interpolated measurement data into the FCNN, which predicts results through its outstanding ability to fit complex model relationships.

Plant growth is primarily determined by two factors: nutrients and energy. Soil is the main source of nutrients for plants [55], while sunlight provides the energy for photosynthesis [56]. These are the fundamental conditions for plant growth and are decisive fac-tors for the plant growth environment. Changes in elevation contain information about changes in surface slope and aspect, which in turn represent changes in soil water and nutrient elements to some extent [57–59]. Information about plant height includes data on plant types and also on the three-dimensional density distribution. These indicators reflect to some extent the competitive relationships for resources among plants and also determine plant growth to a certain extent [60]. Considering the limitations of workload and equipment availability, this study has chosen to collect and measure only a subset of green space attributes.

CEDGAN focuses on soil pH as its training target, while the FCNN employs the Normalized Difference Vegetation Index (NDVI) values as reference outputs for the quality of plant growth environments, incorporating soil parameters (moisture content, salinity, pH, texture), elevation, plant height, and solar radiation energy as input features.

2. Materials and Methods

2.1. Study Area

The study region of this research project is located in the West Lake District of Hangzhou City, Zhejiang Province, China. The study region spans a considerable extent from north to south, which encompasses diverse terrains and environments. The communities residing in this region were established over various periods, which renders the collected data more diverse and representative. This enhances the generalizability and representativeness of the model. We selected urban green spaces within the study area for research based on factors such as time of community establishment, density, surrounding environment, and corresponding regulatory restrictions. The specific distribution of the plots is illustrated in Figure 1. Sample site details can be seen in the example RGB image (Figure 2).

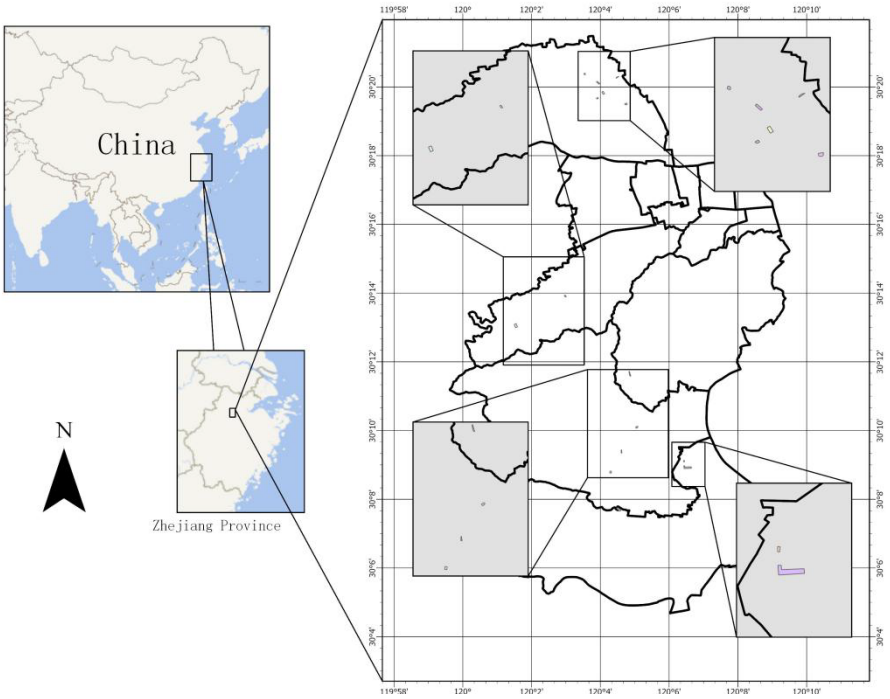

Figure 1. Schematic diagram of the sample plot. (The gray area in the image is a further magnification of the white map, and the colored plots within the gray map represent the sample plots used in this study).

Figure 2. Aerial view of sampling plots. (This image is an actual aerial photograph of the sample plot).

2.2. Data Gathering

2.2.1. Sample Collection and Measurement Methods

In this study, soil samples were collected with a soil sampler (brand: Siyang; product-number: 001; origin: Zhejiang, China) having a diameter of 38 mm. The sampling depth was set at 20 cm, maintaining an interval of 6–10 m between each sampling point. The samples were preserved in transparent zip-lock bags for transportation and storage. The

coordinate information of each soil sample was captured using an RTK terminal (CHCNAV T5 PRO; manufacturer: Shanghai Huace Navigation Technology Ltd.; origin: Shanghai, China), with a CGCS2000 coordinate system employed to save and display the location information. The information of each soil sample is presented in Table 1 in the X, Y, Z data format.

Table 1. Examples of sample point data retention.

Number	Y	X	Z	pH
1	3,357,796.483	505,670.308	12.293	7.90

The soil samples were air-dried naturally, crushed, and then sieved through a 2 mm sieve to obtain the samples needed for further testing processes. Given the model's intended application in large-scale data computation in subsequent phases, necessitating a vast amount of empirical data for training purposes, the study opted for readily measurable indicators. These indicators include soil moisture content, salinity, pH, and texture. The methodologies for these measurements reference the procedures outlined in the book by Bao [61].

In this research, point cloud data were acquired using a DJI M300RTK drone (manufacturer: DJI Innovation; origin: Shenzhen, China) equipped with the L1 payload, while multispectral data were gathered with a DJI Phantom 4 RTK (manufacturer: DJI Innovation; origin: Shenzhen, China) in its multispectral version. Data collection was conducted at a relative cruising altitude of 40 m (point cloud density > 354 points/m^2; ground resolution < 1.09 cm), with an image overlap rate of 75%, and with the flight path velocity set at 10 m/s. This is because traditional satellite remote sensing data typically provide lower resolution data [62], which is far from sufficient for the precision required for the individual urban green spaces in this study. In contrast, DJI drones equipped with L1 LiDAR and multispectral cameras can provide data with higher resolution and accuracy. Additionally, these drones are equipped with an RTK positioning system, which maintains the spatial location error within a 5 cm range. The L1 LiDAR also features inertial navigation system calibration, further enhancing the spatial accuracy of the data.

The samples and data used in the study were collected in July 2023. The overall flow is shown in Figure 3.

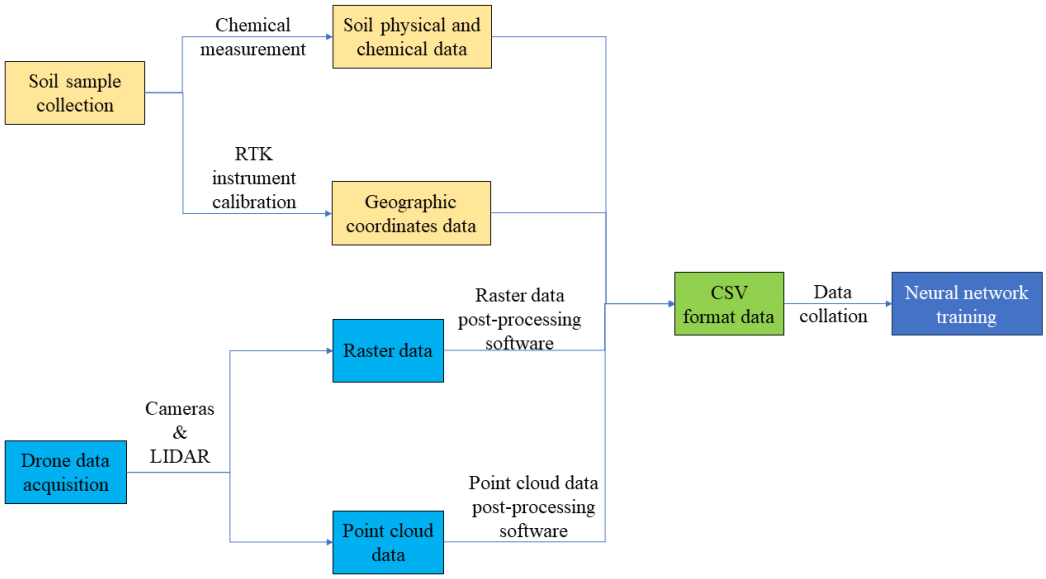

Figure 3. Data processing flowchart.

2.2.2. Data Preprocessing

The soil sample data were saved in CSV files (Table 1), facilitating their reading with Python and subsequent processing in ArcGIS Pro 3.1.

For the training of the CEDGAN network, soil pH data were subjected to preprocessing using the "Data" module in ArcGIS Pro, which facilitated the screening and elimination of anomalously high or low readings, effectively removing outliers and inaccuracies. This was followed by the application of the "Point to Raster" tool for the conversion of the processed data into raster format, with a designated pixel size of 10 and the raster values determined by calculating the average. The final stage involved exporting the rasterized data files from ArcGIS Pro, adjusting the pixel size to 1 to align with the input size requirements of the model, as detailed in Figure 4. The even distribution of the sampling points is impossible at a fixed distance keeping in view the constraints of terrain and other conditions in real-world settings. Additionally, the density and spacing of the sampling points may vary in actual applications. The raster file will be cropped using a Python script according to different sizes (square with sides of 32 and 64 pixels). The 100 or 50 pixels will be randomly sampled as control points in each training sample before training the model. The training samples required are shown in Figure 5.

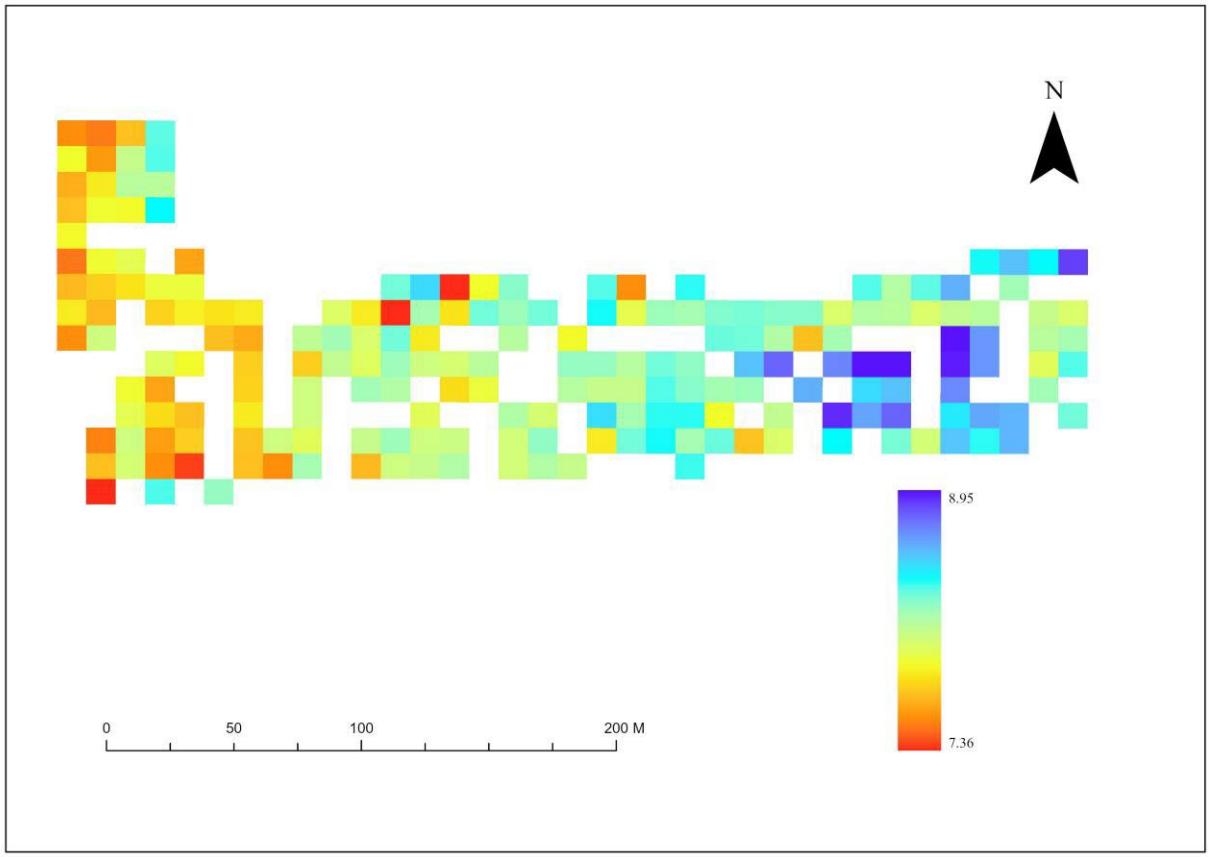

Figure 4. Example of converted raster data. (The variation from deep red to deep blue represents an increase in value, while white areas indicate the absence of data.; each colored square represents a parcel with a side length of 10 m).

The dataset utilized for the training of the FCNN was processed through ArcGIS Pro 3.1, whereby raster data were extracted to the sample points and subsequently exported in CSV format for training purposes. In this study, soil textures are classified into three discrete categories: clayey, loamy, and sandy. To ensure computational balance during the model training phase, soil texture data were subjected to one-hot encoding [63] via a Python script. Furthermore, to align with the characteristics of the ReLU activation function

used during the neural network training phase, NDVI values were normalized to a range of 0 to 1 using min–max normalization through a Python script.

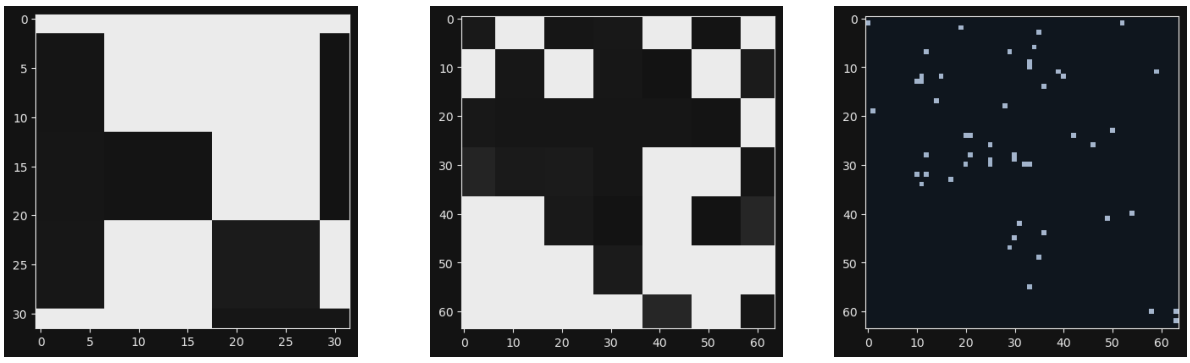

(**a**): 32-pixel edge length training raster (**b**): 64-pixel edge length training raster (**c**): Sample model control points

Figure 5. Raster map of different sizes and control points. (Horizontal and vertical coordinates in pix; the gray scale transformation maps the size of the point values).

Raw point cloud data were processed using DJI Terra software (V3.9.4) to obtain the initial three-dimensional point cloud data for the plot. Subsequently, Cloud Compare (V2.13) was employed to eliminate unnecessary points, resulting in the final point cloud dataset for the plot. This data was then converted into an elevation raster dataset with a pixel resolution of 1 m using ArcGIS Pro 3.1. Utilizing the aforementioned datasets, plant height data and annual solar radiation raster data were calculated through ArcGIS Pro 3.1. In parallel, multispectral imagery data was processed with DJI Terra to derive the Normalized Difference Vegetation Index (NDVI) values for the plot.

Before inputting into the model, the image raster data were normalized to a range of 0 to 1 using Z-score normalization. Since other data values are all greater than zero, and in order to reduce the complexity and computational load of data preprocessing in subsequent model usage, as well as to enhance the model's applicability, other data were only subjected to basic data cleaning without normalization.

2.3. Network Training

2.3.1. Introduction to the Network

The main structure of CEDGAN is depicted in Figure 6a. CEDGAN consists of a generator G and a discriminator D, with the aim of learning the relationship between the sampled spatial data and corresponding real spatial data to generate fake spatial data that are as accurate as possible. D attempts to capture the correspondence between the spatial data and sampled data, to determine whether the interpolated fake data can be considered correct based on a limited number of samples.

In Figure 6b, the details of G and D are displayed. The generator G is designed as a fully convolutional encoder structure, containing three two-dimensional convolutional layers as encoders (convolutional layers 1, 2, and 3) and three two-dimensional transposed convolutional layers as decoders (deconvolutional layers 1, 2, and 3). Each encoder layer performs zero-padded convolution with given kernels and strides. Each decoder layer achieves up-sampling of feature mappings via transposed convolutions with fractional strides, with settings identical to the encoder layers. The discriminator D is a convolutional neural network, akin to typical image classification models. The model employs the concatenation operation to merge the sampled data and full-sized real data (or fake data) as inputs. Each layer of D performs zero-padded convolution once with the settings identical to those of the encoder layers in G. The output of D is a scalar, indicating whether the input full-sized image is a correct interpolation.

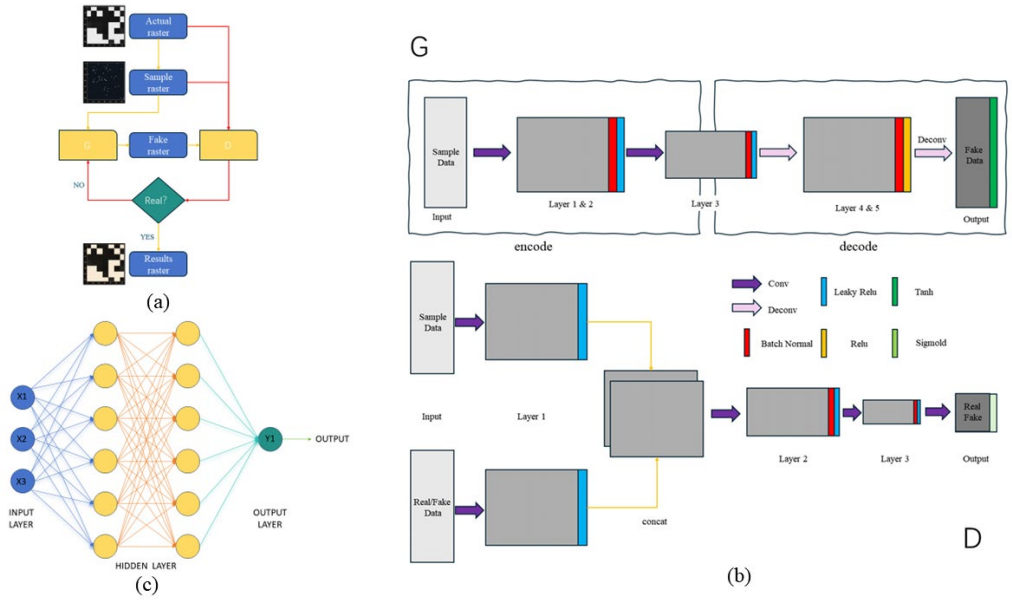

Figure 6. Schematic diagram of the network structure. (**a**) The diagram shows the structure of CEDGAN; (**b**) the diagram provides detailed explanations of G (generator) and D (discriminator) in (**a**); (**c**) the diagram illustrates the structure of the FCNN; different colored lines in the diagram represent different data processing flows.

The primary architecture of the fully connected neural network (FCNN) is depicted in Figure 6c, consisting of an input layer, several hidden layers, and an output layer. The input layer is tasked with receiving raw data and forwarding it to the subsequent layer, with the number of neurons in this layer determined by the quantity of input features. The hidden layers serve as the intermediary stages within the FCNN, with their quantity being flexible. The number of neurons within each hidden layer can be adjusted freely, with each neuron interconnected with all neurons from both the preceding and succeeding layers. The output layer, constituting the terminal stage of the FCNN, is responsible for delivering the network's predictive outcomes, with the number of neurons in this layer dependent on the specific requirements of the task at hand. Each neuron is equipped with an activation function, incorporating nonlinear elements into the network, thereby enabling the FCNN to approximate complex nonlinear relationships.

2.3.2. Training Environment and Parameter Settings

The model was trained in a PyTorch [64] environment under an Anaconda [65] virtual environment, with the versions of PyTorch and CUDA being 2.1.0 and 12.1, respectively. The computational CPU used was Intel i9-13900k, and the GPU was NVIDIA RTX 4090. The operating system was Win11 Pro, and Python scripts were written using PyCharm 2023.1.2.

The CEDGAN training parameters were set with reference to Zhu's research study [43], making appropriate modifications to suit the training set of this study. The network was trained with the mini-batch stochastic gradient descent (SGD) method [66], with a batch size of 64. The training dataset containing raster images was randomly batched, with each batch containing 64 images (batches with fewer than 64 images were discarded). We set the slope to 0.2 for the LeakyReLU [67] activation layer. Moreover, we utilized the Adam optimizer [68], with $\beta 1$ set to 0.5, $\beta 2$ set to 0.999, and the learning rate α for backpropagation set to 0.0002. To ensure consistency in training parameters across different sessions, the random seed in the code related to this study was uniformly set to 999. The PyTorch tensorboard module was used to record relevant losses during training, and this module was employed to visualize the parameters of the training process.

In the configuration of the fully connected neural network (FCNN), the number of nodes in the input layer is tailored to match the count of input features, set specifically

at 9. The architecture includes three hidden layers, with the number of output nodes adjustable based on the requirements of the application. The output layer is defined with a singular node. Throughout the training phase, the random seed is fixed at 66 to ensure reproducibility. The rectified linear unit (ReLU) function is employed as the activation function to introduce nonlinearity, facilitating the model's ability to capture complex relationships. Loss calculation is conducted using the mean squared error loss (MSELoss) method. Optimization is achieved through the Adagrad optimizer, with the learning rate and weight decay parameters set at 0.001 and 0.0001, respectively.

This study employed hold-out cross-validation. The training and test sets were randomly divided in an 8:2 ratio using PyTorch's DataLoader statement.

3. Results

3.1. Overview of Training Dataset

Following meticulous selection, the soil pH dataset employed in the CEDGAN training encompasses a total of 1328 samples, each comprising both GPS coordinates and pH values. A brief overview of this dataset is presented in Table 2. The total of 1432 grid training samples were derived from the above samples. A total of 1163 samples have the dimension of 32 pixels in edge length (Figure 6a), and 269 samples have the dimension of 64 pixels in edge length (Figure 6b). Random rotation was employed during the import process of the 64-pixel edge length model training set due to the limited size of the larger training dataset. This has expanded the number of features for training to approximate the quantity level of smaller-sized samples.

Table 2. Statistical indicators of training data.

Indicators	Mean	Median	Std	Max	Min
pH	7.52	7.86	0.91	8.90	4.82
Water Content	0.175	0.180	0.045	0.38	0.02
Salinity Content	0.093	0.090	0.017	0.41	0.07
Elevation (m)	25.08	20.08	11.52	62.94	10.53
Plant Height (m)	3.57	1.80	4.40	23.10	0.00
Solar Radiation (kWh/m^2)	896.72	936.56	348.78	1540.53	42.87
Corrected NDVI	0.73	0.78	0.17	0.95	0.01

Upon completing a meticulous selection process, the dataset designated for FCNN training comprises 1210 distinct groups. This dataset incorporates a myriad of critical factors, such as the texture of the soil, its moisture and salt content, pH, the altitude at the specific locations where the samples were collected, the stature of the vegetation present, the total solar radiation received over the course of a year, and the values of the NDVI following a process of re-standardization. For a detailed summary of this data, refer to Table 2.

3.2. CEDGAN Training Results

3.2.1. Loss Metrics in CEDGAN Training

Figure 7 exhibits the overall MSE loss between the discriminator and real vs. generated data which reveals a decreasing trend as the number of training iterations increased. However, there are noticeable upward fluctuations at specific epochs. Conversely, the generator's loss has displayed an upward trend with epochs and shows considerable fluctuations at particular epochs. As a whole, the loss varied significantly within the first 20% of the epochs and then gradually stabilized. The MSE loss between the generated and real data was generally below 0.005. The average pixel pH value error was between the two and was below 0.03. The three types of loss fluctuations generally corresponded with

each other, comparing across four sets of training parameters, and usually occurred within the same epoch. The larger-sized samples demonstrated a relatively larger training loss compared with the model training parameters with variable sample size. Furthermore, the amplitude of loss changed with the rise in training epochs and was less pronounced for larger samples. It can be inferred from contrasting the original data curves that the loss fluctuation range during training with smaller samples was more than with larger samples.

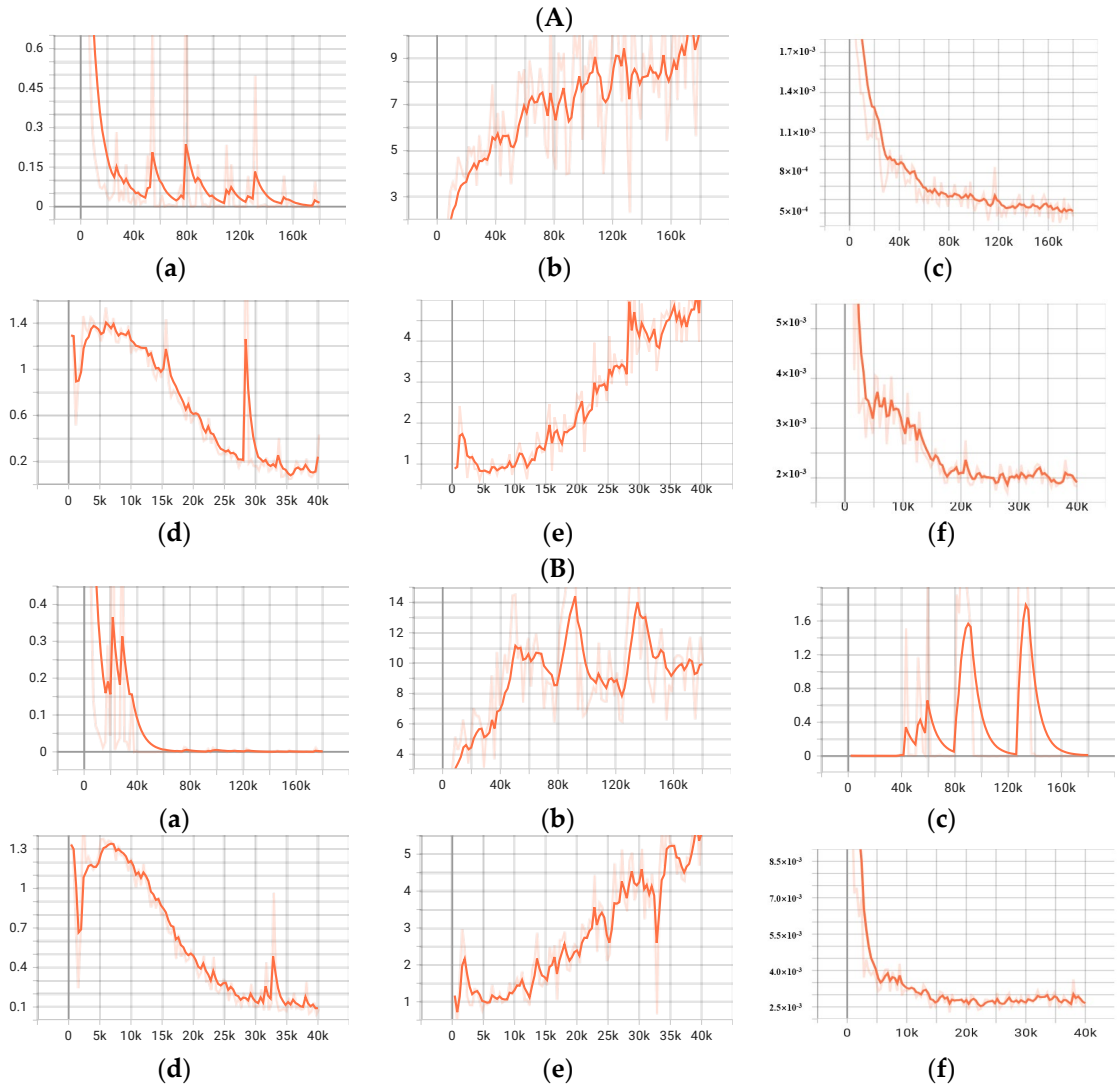

Figure 7. Indicators of model training under different size samples (**A**,**B** represents 100 and 50 sample points); (**a**,**d**) denotes the D loss of 32- and 64-pixel samples; (**b**,**e**) denotes the G loss of 32- and 64-pixel samples; (**c**,**f**) denotes the MSE loss of 32- and 64-pixels samples. Horizontal coordinates are the number of training times; light-colored curves are the original data; dark-colored curves are the curves after smoothing the original data by a factor of 0.8.

In the context of different sampling numbers, the loss during the training process for 32-pixel edge length samples revealed significant discrepancies. The discriminator's loss in the condition of 50 sampling points experienced more pronounced fluctuations initially, but the fluctuations were dramatically reduced later on, almost reaching zero compared to the 100 sampling points. Simultaneously, when the discriminator's loss exhibited considerable fluctuations, the generator's loss halted its rising trend and started to fluctuate considerably. The MSE loss was initially stabilized and was adjacent to zero but later on showed significant fluctuations when the generator's loss varied considerably.

The overall trend was similar to the scenario of 100 sampling points for 64-pixel edge length samples in the condition of 50 sampling points. However, minor fluctuation was more moderate in the 50 sampling points. Meanwhile, both the generator and MSE losses were relatively higher.

3.2.2. Interpolation Performance of CEDGAN on Soil pH

Figure 8 indicates that in general, during the training process, the results of the generator based on the control points gradually approached those of the real samples as the epochs were enhanced. The initial generated images did not present any distinct features, mostly appearing as randomly distributed points. Some connected points became apparent by epoch 20. The small random patches with higher pixel value boundaries began to emerge by epoch 40. Most of these points disappeared by epoch 120. More contiguous and homogeneous patches were produced by epoch 380, and their shape closely resembled the real data. The regularly distributed pixels with higher values started appearing within these uniform patches by epoch 400. The continuous patches began to showcase complex boundaries and value differential areas from epoch 600 onwards. The generated results closely reflected the real samples by epoch 10,000.

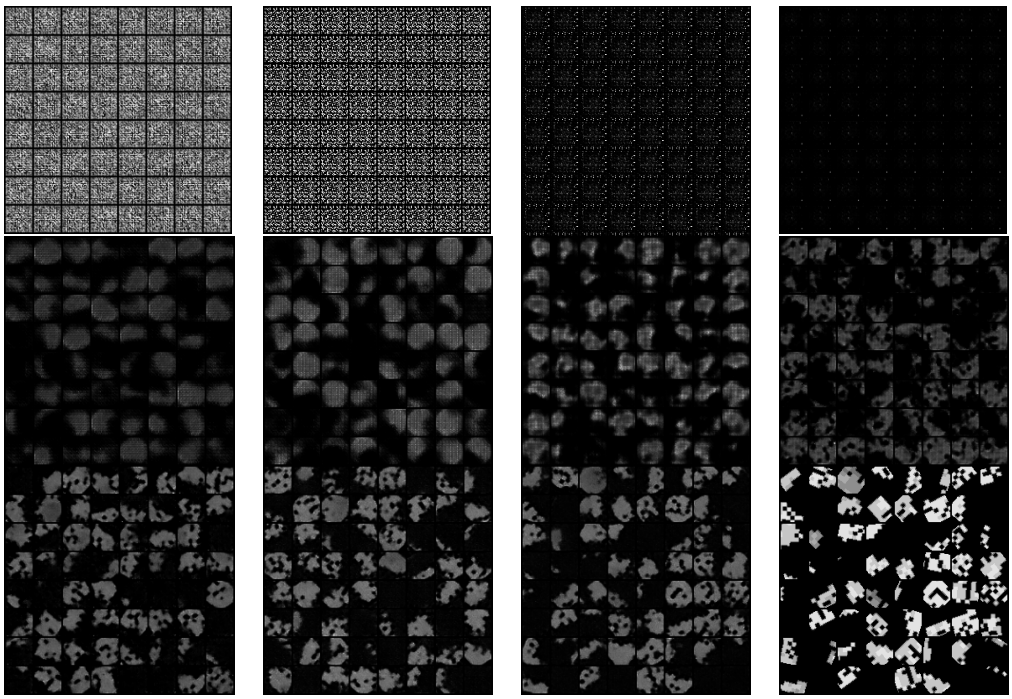

Figure 8. Generator generation results under different epochs during the training process (arranged in order from left to right, top to bottom. Represented are epochs 1, 20, 40, 120, 380, 400, 600, 1400, 5000, 7200, 10,000 and real data samples. The training conditions for the depicted model involve samples with a side length of 64 pixels, with 100 sampling points per sample).

The original data were segmented with a sliding window approach to produce a new dataset and input into the model trained until the last epoch. Figure 9 exhibits that models trained with smaller samples and fewer sampling points were outperformed by those trained with larger samples and more sampling points. The performance showed a trend of improvement with increasing sample size and sampling number.

The generated results showed a minimal resemblance to the real samples, displaying regular patches and some concentrated regions of higher pixel values for the 32-pixel edge length samples trained under the condition of 50 sampling points. The model's generated results, in terms of large-scale structure and distribution, resembled the real samples more closely with 100 sampling points. However, significant discrepancies persisted in the details, with generated images primarily composed of nearly identical pixel values,

appearing relatively smooth, and lacking representation for internal variations within real data patches.

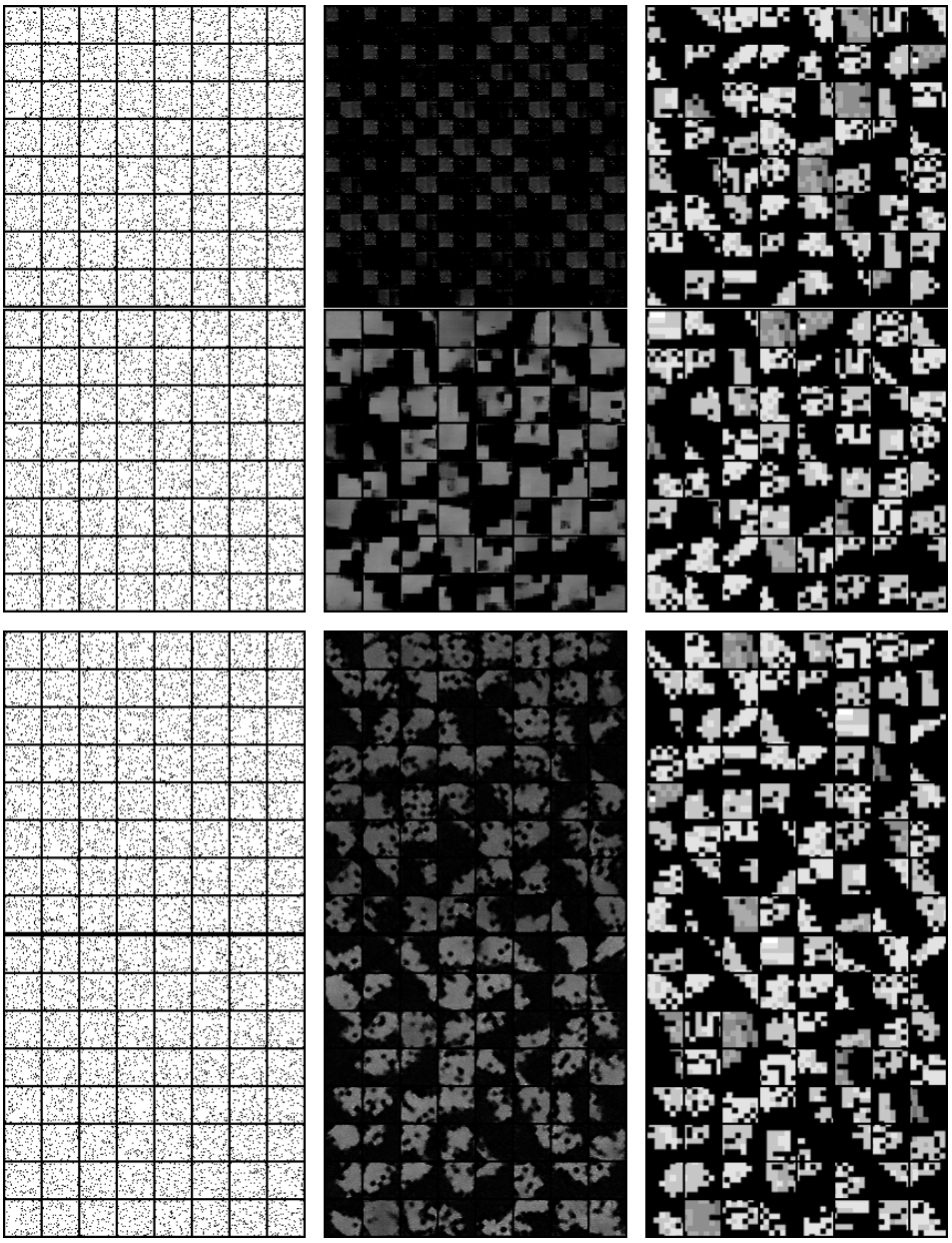

Figure 9. Generation results of different training models for the same sample. The different columns from left to right represent sample points, generated maps, and real samples, respectively; the different rows from top to bottom represent models trained on 32-pixel 50 sample points, 32-pixel 100 sample points, 64-pixel 50 sample points, and 64-pixel 100 sample points, respectively.

The generated results for 64-pixel edge length samples trained under the condition of 50 sampling points surpassed those trained with 32-pixel edge samples. The shape and distribution closely resembled those of the real samples, and internal variations were consistent with the real samples. However, predictions at rapidly changing angles and boundaries were suboptimal, appearing overly smooth.

The best-performing model was trained with 64-pixel edge length samples under the condition of 100 sampling points. The distribution maps predicted by this model, in terms of shape, distribution, magnitude, and variations, were very closely aligned with the real samples.

3.3. FCNN Training Results

Figure 10 reveals that, across all configurations, loss values generally decline as the number of training iterations increases; however, the pace of this decline and the final steady state exhibit distinct differences among configurations. This is manifested by a slower reduction speed in loss values and reduced stability as the number of hidden layers increases, although the loss gradually decreases after the first training session concludes. Similarly, with an increase in the number of nodes per layer, the reduction speed of loss values decelerates, and stability lessens, with an initial increase in loss at the early stages of training. These trends are more pronounced in the training set losses. The model's tendency towards overfitting gradually intensifies with more hidden layers, as indicated by the training set loss falling below the validation set loss at earlier epochs.

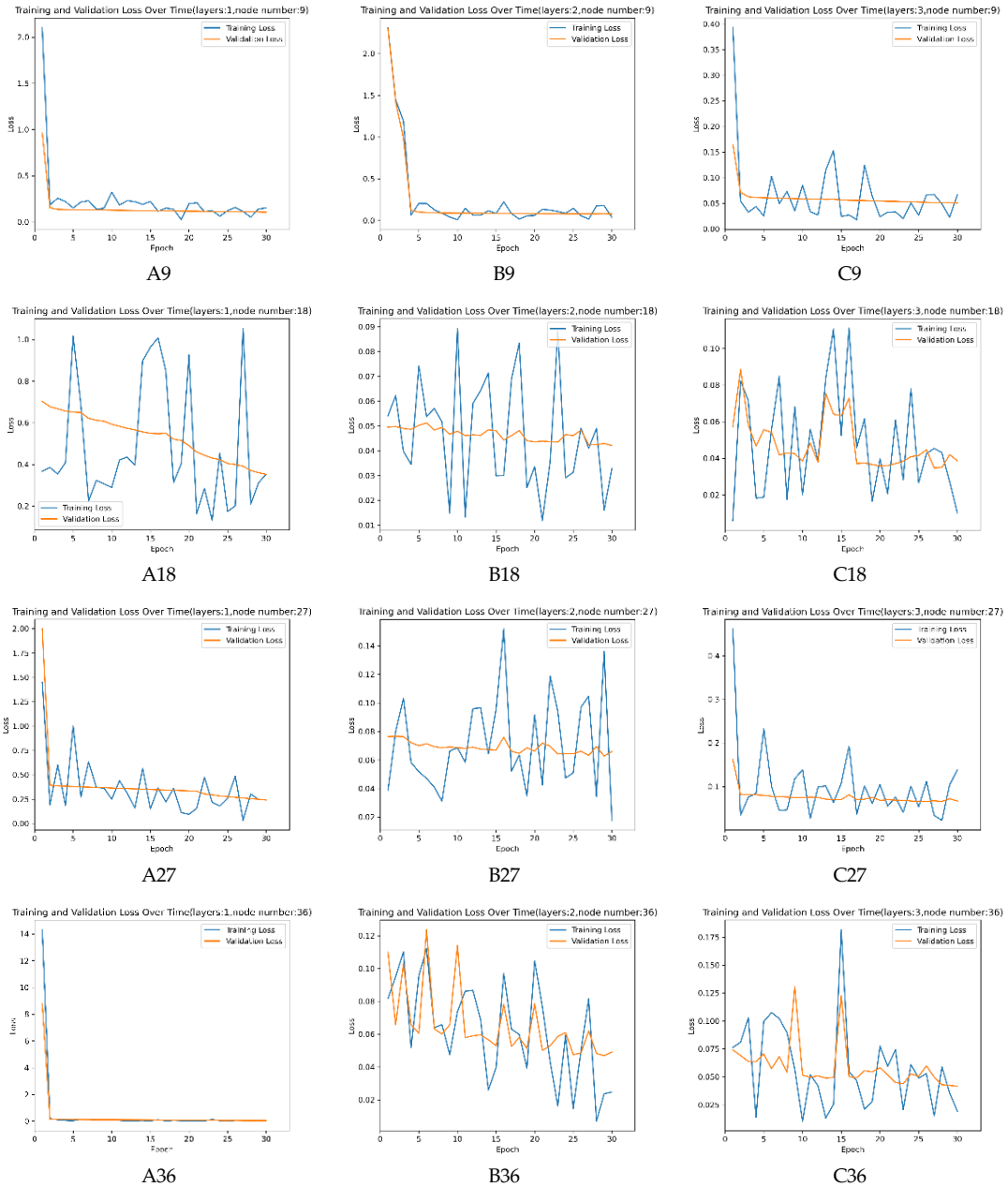

Figure 10. Training loss results for the FCNN network. (Numbers A, B, and C represent the number of hidden layers 1, 2, and 3, respectively; the numbers that follow indicate the number of nodes in each hidden layer).

When there is only one hidden layer, increasing the number of nodes initially reduces then increases the initial loss, hitting its lowest when the node count is 18. However, at 18 and 27 nodes, the training set loss experiences significant fluctuations, with a relatively apparent trend of overfitting at 18 nodes. With two hidden layers, the initial loss also minimizes at 18 nodes. However, as the number of nodes increases with two hidden layers, the reduction speed of the validation set loss slows, and the fluctuation becomes more pronounced; the training set loss shows nearly completely random variation. With three hidden layers, increasing the number of nodes shows a pattern of initial decrease, followed by an increase and then a decrease in initial loss, with the lowest at 18 nodes. The fluctuation degree of training loss also increases with the number of nodes, showing a pattern of decrease, then increase, and then decrease again.

4. Discussion

Urban planning and environmental management face increasing challenges as urban expansion leads to continuous changes in green spaces [69], and the workload also increases accordingly. Therefore, a method that can quickly assess the quality of urban green spaces is needed. Moreover, due to the growing demand for urban green spaces in envi-ronmental protection and other areas [70–72], a method that provides more accurate, precise, and economical data collection is necessary. However, due to the complexity of urban environments, this task presents significant challenges [45–47]. This study combines neural networks and drone remote sensing technologies, planning to provide a relatively accurate, precise, and economical monitoring system for urban green space quality.

One of the principal objectives of this research study was to interpolate spatial attributes of urban green spaces using CEDGAN. This study has emphasized on interpolation of soil pH values within green spaces.

The majority of our samples displayed signs of convergence during training, gradually optimizing as the epochs progressed. However, it is evident that larger-sized samples showed more significant training loss, with relatively minimal variations in the loss magnitude. This could be attributed to more computational complexity faced by the model when dealing with larger-sized data [73].

The larger datasets usually encapsulate more intricate details and variations, as visualized in Figure 5. This furnishes the GAN's discriminator and generator with richer training data and features. Conversely, smaller-sized samples exhibited more significant fluctuations in training loss, possibly due to their provision of limited information. This can lead to instability during the model's prediction phase, resulting in higher volatility [74].

Significant fluctuations in the loss function at specific cycle counts warrant further investigation. Such fluctuations might arise from mode collapse experienced during GAN training—a well-known issue with GANs. The generator might find ways to deceive the discriminator in certain iterations, leading to such fluctuations [75].

A notable observation from the data is the model's tendency to shift its focus from localized to global information, or vice versa. This might elucidate the substantial shifts in both the generator's and discriminator's loss values in certain cycles. The global trend of generator loss seems contrary to other metrics, potentially resulting from the discriminator's continual optimization and increasing discernment, subsequently elevating the generator's loss [76–78]. This observation is positive, indicating continuous optimization during training.

The limited sample size might ease model convergence but could also precipitate issues like premature convergence to local optima or gradient explosion [79]. Therefore, as evident in the plots (Figure 7), low-sample-density raster data show drastic fluctuations in training loss towards the latter stages. Conversely, higher sample densities supply richer information, aiding the model in learning data distribution and structure more accurately. However, this also escalates computational requirements and feature count, slowing convergence and amplifying loss.

The features learned by the generator gradually deepen with the growing number of epochs, transitioning from rudimentary edge features to complex structures and textures. This sequential learning process exemplifies how deep learning networks progressively extract features, rather than simply memorizing the training samples.

The present study validated the model to assess its generalization capabilities with the dataset obtained from sliding segmentation. It has been observed that different input sizes might affect feature extraction. The smaller inputs might emphasize local features, leading to pixel clusters (Figure 9). The larger inputs might focus on global features. Although every model demonstrated some degree of interpolation capability, the performance was optimal for the models trained with 64-pixel side length samples at 100 sample points. This suggests that adequate context and sample volume are essential for precise predictions.

Even the best-performing models showed some discrepancies in the details compared to the real samples. This suggests that sample size and sample count are only among several factors influencing prediction performance. This is also illustrated by the research of Benkendorf et al. [80]. Other factors such as optimizer selection, learning rate strategy, etc., might play a role. The sole reliance on increasing sample size and count might not maximize performance [81]. Further research is recommended to identify optimal model parameters and to enhance accuracy and generalizability.

Another objective of this study was to develop a predictive model for evaluating the growth environments of urban greenery based on nine green space attributes, utilizing the FCNN. Throughout the training phase, a gradual decline in loss values was observed as the number of training iterations increased, indicative of the model's capability to learn and adapt to the data's characteristics. The variance in the trend of decreasing loss values and the ultimate stabilization state under different network architectures underscored the significant impact of model structural parameters on training efficiency and performance. These phenomena can be attributed, on the one hand, to a mismatch between model complexity and the volume of training data, leading to overfitting [82]. On the other hand, the initial increase in loss values may stem from the high variance caused by the random initialization of model parameters at the outset [83]. This aligns with recent studies, suggesting that the design and optimization of deep learning models are crucial for enhancing predictive performance [84].

Increasing the number of hidden layers was observed to slow down the loss reduction trend and decrease model stability, potentially reflecting overfitting issues due to increased model complexity, as indicated in recent research. Overfitting significantly impairs the model's generalization ability on unseen data [85]. Furthermore, our findings suggest that increasing the number of nodes per layer, particularly in configurations with more hidden layers, intensifies the model's tendency towards overfitting, further affirming that excessively increasing model complexity can negatively impact training efficiency and model generalizability.

Overfitting is a common problem in deep learning, especially when the model complexity is high and the training samples are limited. He [86] pointed out that overfitting can be effectively mitigated by increasing the amount of data, using data augmentation techniques, or introducing regularization terms (such as L1/L2 regularization, dropout). For the issue of loss value increase at the beginning of training, Glorot and Bengio [83] have recommended using appropriate weight initialization strategies, like Xavier initialization, to improve the stability of model training in its initial phase.

In this study, the depth of the hidden layers and the number of nodes per layer significantly impacted model performance. The research conducted by Srivastava [87] demonstrates how dropout, as a regularization technique, effectively reduces overfitting and enhances the model's generalization capability on unseen data. Hence, introducing dropout could be an effective solution to address the increased fluctuations in loss values with an increase in the number of nodes.

To tackle the issues of overfitting caused by the addition of hidden layers and the slowed rate of loss value decrease, the adoption of more sophisticated regularization

techniques, such as batch normalization [88], could be considered. This approach not only accelerates the training process but also enhances the model's stability and performance.

The high-precision spatial interpolation capabilities of CEDGAN make it particularly effective in handling complex urban environmental data, directly enhancing the accuracy of future urban planning and environmental monitoring models. Meanwhile, the strong fitting ability of the FCNN enables it to effectively process and predict multi-dimensional nonlinear relationships, which is significant for in-depth analysis of environmental data and the development of more complex models in the future.

Moving forward, we plan to further refine and optimize these research findings to better adapt to the actual management needs of urban green spaces. For example, we are considering developing a comprehensive model that can simultaneously handle the interpolation of multiple spatial attributes such as soil NPK values, moisture, and sunlight, to provide more comprehensive data support. Additionally, we are exploring ways to increase the model's interpretability, so that managers can more intuitively understand the basis of the model's predictions.

Overall, this study highlights the potential of CEDGAN in interpolating urban green space attributes and the FCNN in predicting and evaluating plant growth performance. However, it also uncovers the challenges faced during their training processes. Future work could delve into exploring alternative network architectures or employing additional data augmentation techniques to enhance the models' stability and predictive accuracy, and on this basis, develop more models. Moving forward, we hope that these network structures can be widely applied to more environmental science and urban development studies.

5. Conclusion

The following is concluded:

(1) CEDGAN can be effectively employed for the interpolation of spatial attributes in urban green spaces. The per-pixel average error was found to be less than 0.03 for the prediction of pH values;
(2) The efficacy of CEDGAN in urban green space interpolation was significantly influenced by training sample size, with larger samples yielding better results;
(3) The effectiveness of CEDGAN in urban green space interpolation was substantially affected by the number of sample points, with higher sample counts leading to superior results;
(4) The CEDGAN network requires more samples with high information density to enhance performance and accuracy for the interpolation of urban green spaces;
(5) The FCNN model exhibits strong performance in evaluating and predicting plant growth environments, with general prediction errors less than 0.1;
(6) When comparing network structures with various parameters, those FCNN models with fewer hidden layers and nodes demonstrate superior training outcomes.

Author Contributions: Y.W. and Z.M.: conceptualization, analysis and model validation, writing—original draft. H.J. and D.L.: resources and supervision. Z.W.: data curation. A.S.: proofreading and English inspection. All authors contributed to the article and approved the submitted version. All authors have read and agreed to the published version of the manuscript.

Funding: This work was supported by the Special Support Program for High-level Talents in Zhejiang Province [Grant number 2020R52026]. The funding recipient is D.L.

Data Availability Statement: Data will be made available on request. The code and some of the data used in this study can be downloaded from our Github site. https://github.com/IMWNIIP/Spatial-interpolation-of-urban-green-space (accessed on 18 November 2023).

Acknowledgments: This work used the CEDGAN model. This model was open-sourced by Zhu et al. in 2019 [43].

Conflicts of Interest: The authors declare no conflict of interest.

References

1. Addas, A. The Importance of Urban Green Spaces in the Development of Smart Cities. *Front. Environ. Sci.* **2023**, *11*, 1206372. [CrossRef]
2. Aronson, M.F.; Lepczyk, C.A.; Evans, K.L.; Goddard, M.A.; Lerman, S.B.; MacIvor, J.S.; Nilon, C.H.; Vargo, T. Biodiversity in the City: Key Challenges for Urban Green Space Management. *Front. Ecol. Environ.* **2017**, *15*, 189–196. [CrossRef]
3. Atiqul Haq, S.M.; Islam, M.N.; Siddhanta, A.; Ahmed, K.J.; Chowdhury, M.T.A. Public Perceptions of Urban Green Spaces: Convergences and Divergences. *Front. Sustain. Cities* **2021**, *3*, 755313. [CrossRef]
4. Niemelä, J. Ecology of Urban Green Spaces: The Way Forward in Answering Major Research Questions. *Landsc. Urban Plan.* **2014**, *125*, 298–303. [CrossRef]
5. Han, J.-G.; Li, G.; Zhang, W.-W.; Liu, W.; Liu, S.; Ma, X.; Zhang, L.; Zhu, Y.-G. Problems and Countermeasures of Soil Health Quality in Urban Green Space. *Ying Yong Sheng Tai Xue Bao J. Appl. Ecol./Zhongguo Sheng Tai Xue Xue Hui Zhongguo Ke Xue Yuan Shenyang Ying Yong Sheng Tai Yan Jiu Suo Zhu Ban* **2022**, *33*, 268–276. [CrossRef] [PubMed]
6. Li, N.; Liu, Y. Sustainable Design in Urban Green Space. In *Sustainability in Urban Planning and Design*; IntechOpen: Rijeka, Croatia, 2019. [CrossRef]
7. Knobel, P.; Dadvand, P.; Alonso, L.; Costa, L.; Español, M.; Maneja, R. Development of the Urban Green Space Quality Assessment Tool (RECITAL). *Urban For. Urban Green.* **2020**, *57*, 126895. [CrossRef]
8. Stessens, P.; Canters, F.; Huysmans, M.; Khan, A.Z. Urban Green Space Qualities: An Integrated Approach towards GIS-Based Assessment Reflecting User Perception. *Land Use Policy* **2020**, *91*, 104319. [CrossRef]
9. Pudifoot, B.; Cárdenas, M.L.; Buytaert, W.; Paul, J.D.; Narraway, C.L.; Loiselle, S. When It Rains, It Pours: Integrating Citizen Science Methods to Understand Resilience of Urban Green Spaces. *Front. Water* **2021**, *3*, 654493. [CrossRef]
10. Martins, R.N.; Ferreira Lima Dos Santos, F.; Araújo, G.D.M.; Viana, L.D.A.; Rosas, J.T.F. Accuracy Assessments of Stochastic and Deterministic Interpolation Methods in Estimating Soil Attributes Spatial Variability. *Commun. Soil Sci. Plant Anal.* **2019**, *50*, 2570–2578. [CrossRef]
11. Chouksey, N.; Mishra, G.C.; Chouksey, R. GIS-Based Interpolation Methods for Estimating Spatial Distribution of Nitrogen Content in the Soil. *J. Krishi Vigyan* **2018**, *7*, 78. [CrossRef]
12. Qiao, P.; Lei, M.; Yang, S.; Yang, J.; Guo, G.; Zhou, X. Comparing Ordinary Kriging and Inverse Distance Weighting for Soil as Pollution in Beijing. *Environ. Sci. Pollut. Res.* **2018**, *25*, 15597–15608. [CrossRef] [PubMed]
13. Cleemput, E.V.; Vanierschot, L.; Fernández-Castilla, B.; Honnay, O.; Somers, B. The Functional Characterization of Grass- and Shrubland Ecosystems Using Hyperspectral Remote Sensing: Trends, Accuracy and Moderating Variables. *Remote Sens. Environ.* **2018**, *209*, 747–763. [CrossRef]
14. Degerickx, J.; Hermy, M.; Somers, B. Mapping Functional Urban Green Types Using High Resolution Remote Sensing Data. *Sustainability* **2020**, *12*, 2144. [CrossRef]
15. Pandey, P.C.; Balzter, H.; Srivastava, P.; Petropoulos, G.; Bhattacharya, B. Future Perspectives and Challenges in Hyperspectral Remote Sensing. *Hyperspectral Remote Sens.* **2020**, 429–439. [CrossRef]
16. Chen, W.; Huang, H.; Dong, J.; Zhang, Y.; Tian, Y.; Yang, Z. Social Functional Mapping of Urban Green Space Using Remote Sensing and Social Sensing Data. *ISPRS J. Photogramm. Remote Sens.* **2018**, *146*, 436–452. [CrossRef]
17. Neyns, R.; Canters, F. Mapping of Urban Vegetation with High-Resolution Remote Sensing: A Review. *Remote Sens.* **2022**, *14*, 1031. [CrossRef]
18. Shahtahmassebi, A.; Li, C.; Fan, Y.; Wu, Y.; Lin, Y.; Gan, M.; Wang, K.; Malik, A.; Blackburn, G.A. Remote Sensing of Urban Green Spaces: A Review. *Urban For. Urban Green.* **2021**, *57*, 126946. [CrossRef]
19. Cui, R.; Hu, Z.; Wang, P.; Han, J.; Zhang, X.; Jiang, X.; Cao, Y. Crop Classification and Growth Monitoring in Coal Mining Subsidence Water Areas Based on Sentinel Satellite. *Remote Sens.* **2023**, *15*, 5095. [CrossRef]
20. Heidarian Dehkordi, R.; Burgeon, V.; Fouche, J.; Placencia Gomez, E.; Cornelis, J.-T.; Nguyen, F.; Denis, A.; Meersmans, J. Using UAV Collected RGB and Multispectral Images to Evaluate Winter Wheat Performance across a Site Characterized by Century-Old Biochar Patches in Belgium. *Remote Sens.* **2020**, *12*, 2504. [CrossRef]
21. Yu, H.; Kong, B.; Hou, Y.; Xu, X.; Chen, T.; Liu, X. A Critical Review on Applications of Hyperspectral Remote Sensing in Crop Monitoring. *Exp. Agric.* **2022**, *58*, e26. [CrossRef]
22. Orengo, H.A.; Petrie, C.A. Large-Scale, Multi-Temporal Remote Sensing of Palaeo-River Networks: A Case Study from Northwest India and Its Implications for the Indus Civilisation. *Remote Sens.* **2017**, *9*, 735. [CrossRef]
23. Xu, Z.; Zhou, Y.; Wang, S.; Wang, L.; Li, F.; Wang, S.; Wang, Z. A Novel Intelligent Classification Method for Urban Green Space Based on High-Resolution Remote Sensing Images. *Remote Sens.* **2020**, *12*, 3845. [CrossRef]
24. Liu, Y.; Pan, X.; Liu, Q.; Li, G. Establishing a Reliable Assessment of the Green View Index Based on Image Classification Techniques, Estimation, and a Hypothesis Testing Route. *Land* **2023**, *12*, 1030. [CrossRef]
25. Zhang, X.; Zhang, F.; Qi, Y.; Deng, L.; Wang, X.; Yang, S. New Research Methods for Vegetation Information Extraction Based on Visible Light Remote Sensing Images from an Unmanned Aerial Vehicle (UAV). *Int. J. Appl. Earth Obs. Geoinf.* **2019**, *78*, 215–226. [CrossRef]
26. Rouse, J.W.; Haas, R.H.; Schell, J.A.; Deering, D.W. *Monitoring Vegetation Systems in the Great Plains with ERTS*; NASA Special Publications: Springfield, VA, USA, 1973.

27. Huang, S.; Tang, L.; Hupy, J.P.; Wang, Y.; Shao, G. A Commentary Review on the Use of Normalized Difference Vegetation Index (NDVI) in the Era of Popular Remote Sensing. *J. For. Res.* **2021**, *32*, 1–6. [CrossRef]
28. Geerken, R.; Zaitchik, B.; Evans, J.P. Classifying Rangeland Vegetation Type and Coverage from NDVI Time Series Using Fourier Filtered Cycle Similarity. *Int. J. Remote Sens.* **2005**, *26*, 5535–5554. [CrossRef]
29. Lin, X.; Niu, J.; Berndtsson, R.; Yu, X.; Zhang, L.; Chen, X. NDVI Dynamics and Its Response to Climate Change and Reforestation in Northern China. *Remote Sens.* **2020**, *12*, 4138. [CrossRef]
30. Yang, J.; Wan, Z.; Borjigin, S.; Zhang, D.; Yan, Y.; Chen, Y.; Gu, R.; Gao, Q. Changing Trends of NDVI and Their Responses to Climatic Variation in Different Types of Grassland in Inner Mongolia from 1982 to 2011. *Sustainability* **2019**, *11*, 3256. [CrossRef]
31. Wang, X.; Zhao, Y.; Pourpanah, F. Recent Advances in Deep Learning. *Int. J. Mach. Learn. Cybern.* **2020**, *11*, 747–750. [CrossRef]
32. Hochreiter, S.; Schmidhuber, J. Long Short-Term Memory. *Neural Comput.* **1997**, *9*, 1735–1780. [CrossRef]
33. Li, Q.; Zhao, Y.; Yu, F. A Novel Multichannel Long Short-Term Memory Method with Time Series for Soil Temperature Modeling. *IEEE Access* **2020**, *8*, 182026–182043. [CrossRef]
34. Scarselli, F.; Gori, M.; Tsoi, A.C.; Hagenbuchner, M.; Monfardini, G. The Graph Neural Network Model. *IEEE Trans. Neural Netw.* **2009**, *20*, 61–80. [CrossRef] [PubMed]
35. Phung, T.H.; Nguyen, D.L.; Vu, V.H.; Huynh, T.T.; Nguyen, T.H.; Nguyen, P.L. Unsupervised Air Quality Interpolation with Attentive Graph Neural Network. In Proceedings of the 11th International Symposium on Information and Communication Technology, Hanoi, Vietnam, 1–3 December 2022; Association for Computing Machinery: New York, NY, USA, 2022; pp. 103–110.
36. Albawi, S.; Mohammed, T.A.; Al-Zawi, S. Understanding of a Convolutional Neural Network. In Proceedings of the 2017 International Conference on Engineering and Technology (ICET), Antalya, Turkey, 21–23 August 2017; pp. 1–6.
37. Fischer, M.M. Computational Neural Networks: A New Paradigm for Spatial Analysis. *Environ. Plan. A* **1998**, *30*, 1873–1891. [CrossRef]
38. Padarian, J.; Minasny, B.; McBratney, A.B. Using Deep Learning for Digital Soil Mapping. *Soil* **2019**, *5*, 79–89. [CrossRef]
39. Baur, C.; Albarqouni, S.; Navab, N. Semi-Supervised Deep Learning for Fully Convolutional Networks. In *Medical Image Computing and Computer Assisted Intervention—MICCAI 2017: 20th International Conference, Quebec City, QC, Canada, 11–13 September 2017, Proceedings, Part III 20*; Springer International Publishing: Cham, Switzerland, 2017; pp. 311–319. [CrossRef]
40. Shrestha, A.; Mahmood, A. Review of Deep Learning Algorithms and Architectures. *IEEE Access* **2019**, *7*, 53040–53065. [CrossRef]
41. Alzubaidi, L.; Bai, J.; Al-Sabaawi, A.; Santamaría, J.; Albahri, A.S.; Al-dabbagh, B.S.N.; Fadhel, M.A.; Manoufali, M.; Zhang, J.; Al-Timemy, A.H.; et al. A Survey on Deep Learning Tools Dealing with Data Scarcity: Definitions, Challenges, Solutions, Tips, and Applications. *J. Big Data* **2023**, *10*, 46. [CrossRef]
42. Nikparvar, B.; Thill, J.-C. Machine Learning of Spatial Data. *ISPRS Int. J. Geo-Inf.* **2021**, *10*, 600. [CrossRef]
43. Zhu, D.; Cheng, X.; Zhang, F.; Yao, X.; Gao, Y.; Liu, Y. Spatial Interpolation Using Conditional Generative Adversarial Neural Networks. *Int. J. Geogr. Inf. Sci.* **2019**, *34*, 735–758. [CrossRef]
44. Goodfellow, I.; Pouget-Abadie, J.; Mirza, M.; Xu, B.; Warde-Farley, D.; Ozair, S.; Courville, A.; Bengio, Y. Generative Adversarial Networks. *Commun. ACM* **2020**, *63*, 139–144. [CrossRef]
45. Kalfas, D.; Chatzitheodoridis, F.; Loizou, E.; Melfou, K. Willingness to Pay for Urban and Suburban Green. *Sustainability* **2022**, *14*, 2332. [CrossRef]
46. Sun, M.; Zhao, X.; Wang, Y.; Ren, Z.; Fu, X. Factors Affecting the High-Intensity Cooling Distance of Urban Green Spaces: A Case Study of Xi'an, China. *Sustainability* **2023**, *15*, 6735. [CrossRef]
47. Tao, P.; Lin, Y.; Wang, X.; Li, J.; Ma, C.; Wang, Z.; Dong, X.; Yao, P.; Shao, M. Optimization of Green Spaces in Plain Urban Areas to Enhance Carbon Sequestration. *Land* **2023**, *12*, 1218. [CrossRef]
48. Hammer, G.; Cooper, M.; Tardieu, F.; Welch, S.; Walsh, B.; van Eeuwijk, F.; Chapman, S.; Podlich, D. Models for Navigating Biological Complexity in Breeding Improved Crop Plants. *Trends Plant Sci.* **2006**, *11*, 587–593. [CrossRef] [PubMed]
49. Kvamme, H.; Borgan, Ø. Continuous and Discrete-Time Survival Prediction with Neural Networks. *Lifetime Data Anal.* **2019**, *27*, 710–736. [CrossRef] [PubMed]
50. Liquet, B.; Moka, S.; Nazarathy, Y. *Mathematical Engineering of Deep Learning*; CRC Press: Boca Raton, FL, USA, 2024.
51. Dumas, T.; Roumy, A.; Guillemot, C. Context-Adaptive Neural Network-Based Prediction for Image Compression. *IEEE Trans. Image Process.* **2018**, *29*, 679–693. [CrossRef] [PubMed]
52. Luo, J.; Hao, J.; Yang, Y.; Hong, F.; Wang, X.; Ge, Z. Comparison and Evaluation of Multiple Neural Network Models in Wind Power Generation Forecasting. In Proceedings of the 2022 4th International Conference on Smart Power & Internet Energy Systems (SPIES), Beijing, China, 9–12 December 2022; pp. 2087–2092. [CrossRef]
53. Fan, M.; Bai, Y.; Wang, L.; Ding, L. Combining a Fully Connected Neural Network With an Ensemble Kalman Filter to Emulate a Dynamic Model in Data Assimilation. *IEEE Access* **2021**, *9*, 144952–144964. [CrossRef]
54. Maggiori, E.; Tarabalka, Y.; Charpiat, G.; Alliez, P. Fully Convolutional Neural Networks for Remote Sensing Image Classification. In Proceedings of the 2016 IEEE International Geoscience and Remote Sensing Symposium (IGARSS), Beijing, China, 10–15 July 2016; pp. 5071–5074.
55. McGrath, J.; Spargo, J.; Penn, C. Soil Fertility and Plant Nutrition. In *Plant Health*; Elsevier: New York, NY, USA, 2014; pp. 166–184. [CrossRef]
56. Schlesinger, W.; Bernhardt, E. The Biosphere: Biogeochemical Cycling on Land. In *Biogeochemistry*, 3rd ed.; Elsevier: New York, NY, USA, 2013; pp. 173–231. [CrossRef]

57. Adhikari, K.; Owens, P.; Ashworth, A.; Sauer, T.; Libohova, Z.; Richter, J.L.; Miller, D.M. Topographic Controls on Soil Nutrient Variations in a Silvopasture System. *Agrosystems Geosci. Environ.* **2018**, *1*, 1–15. [CrossRef]
58. Sun, J.; Huang, C.-H.; Han, G.; Wang, Y. Effects of Cover on Soil Particle and Associated Soil Nutrient Redistribution on Slopes under Rainfall Simulation. *J. Soils Sediments* **2018**, *19*, 729–740. [CrossRef]
59. Varga, C.; Csiszér, L. The Influence of Slope Aspect on Soil Moisture. *Acta Univ. Sapientiae Agric. Environ.* **2020**, *12*, 82–93. [CrossRef]
60. Malambo, L.; Popescu, S.; Murray, S.; Putman, E.; Pugh, N.A.; Horne, D.W.; Richardson, G.; Sheridan, R.; Rooney, W.; Avant, R.; et al. Multitemporal Field-Based Plant Height Estimation Using 3D Point Clouds Generated from Small Unmanned Aerial Systems High-Resolution Imagery. *Int. J. Appl. Earth Obs. Geoinf.* **2018**, *64*, 31–42. [CrossRef]
61. Bao, S.D. *Soil and Agricultural Chemistry Analysis*; China Agricultural Press: Beijing, China, 2000.
62. Al-Wassai, F.A.; Kalyankar, N. Major Limitations of Satellite Images. *arXiv* **2013**, arXiv:1307.2434.
63. Ashenden, S.K.; Bartosik, A.; Agapow, P.-M.; Semenova, E. Chapter 2—Introduction to Artificial Intelligence and Machine Learning. In *The Era of Artificial Intelligence, Machine Learning, and Data Science in the Pharmaceutical Industry*; Ashenden, S.K., Ed.; Academic Press: Cambridge, MA, USA, 2021; pp. 15–26. ISBN 978-0-12-820045-2.
64. PyTorch Documentation—PyTorch 2.1 Documentation. Available online: https://pytorch.org/docs/stable/index.html (accessed on 14 November 2023).
65. Welcome!—Anaconda Documentation. Available online: https://docs.anaconda.com/ (accessed on 14 November 2023).
66. Bottou, L.; Bousquet, O. *The Tradeoffs of Large Scale Learning. Advances in Neural Information Processing Systems*; MIT Press: Cambridge, MA, USA, 2007; Volume 20.
67. LeakyReLU—PyTorch 2.1 Documentation. Available online: https://pytorch.org/docs/stable/generated/torch.nn.LeakyReLU.html (accessed on 14 November 2023).
68. Adam—PyTorch 2.1 Documentation. Available online: https://pytorch.org/docs/stable/generated/torch.optim.Adam.html (accessed on 14 November 2023).
69. Li, Q.; Thapa, S.; Hu, X.; Luo, Z.; Gibson, D. The Relationship between Urban Green Space and Urban Expansion Based on Gravity Methods. *Sustainability* **2022**, *14*, 5396. [CrossRef]
70. Haq, S. Urban Green Spaces and an Integrative Approach to Sustainable Environment. *J. Environ. Prot.* **2011**, *2*, 601–608. [CrossRef]
71. Yan, S.; Ecological Safety Design of Green Space of Urban Roads. J. *Cent. South Univ. For. Technol.* 2011. Available online: https://api.semanticscholar.org/CorpusID:130592348 (accessed on 14 November 2023).
72. Wolch, J.; Byrne, J.; Newell, J. Urban Green Space, Public Health, and Environmental Justice: The Challenge of Making Cities 'Just Green Enough'. *Landsc. Urban Plan.* **2014**, *125*, 234–244. [CrossRef]
73. Rajput, D.; Wang, W.-J.; Chen, C.-C. Evaluation of a Decided Sample Size in Machine Learning Applications. *BMC Bioinform.* **2023**, *24*, 48. [CrossRef] [PubMed]
74. Vabalas, A.; Gowen, E.; Poliakoff, E.; Casson, A. Machine Learning Algorithm Validation with a Limited Sample Size. *PLoS ONE* **2019**, *14*, e0224365. [CrossRef] [PubMed]
75. Li, W.; Fan, L.; Wang, Z.; Ma, C.; Cui, X. Tackling Mode Collapse in Multi-Generator GANs with Orthogonal Vectors. *Pattern Recognit.* **2021**, *110*, 107646. [CrossRef]
76. Zhou, F.; Yang, S.; Fujita, H.; Chen, D.; Wen, C. Deep Learning Fault Diagnosis Method Based on Global Optimization GAN for Unbalanced Data. *Knowl. Based Syst.* **2020**, *187*, 104837. [CrossRef]
77. Nguyen, C.V.; Cao, T.-D.; Truong-Huu, T.; Pham, K.; Nguyen, B.T. An Empirical Study on GANs with Margin Cosine Loss and Relativistic Discriminator. *arXiv* **2021**, arXiv:2110.11293.
78. Jolicoeur-Martineau, A. The Relativistic Discriminator: A Key Element Missing from Standard GAN. *arXiv* **2018**, arXiv:1807.00734.
79. Liu, K.; Wang, Z.; Wu, L. The Local Landscape of Phase Retrieval Under Limited Samples. *arXiv* **2023**, arXiv:2311.15221. [CrossRef]
80. Benkendorf, D.J.; Hawkins, C. Effects of Sample Size and Network Depth on a Deep Learning Approach to Species Distribution Modeling. *Ecol. Inform.* **2020**, *60*, 101137. [CrossRef]
81. Choi, D.; Shallue, C.J.; Nado, Z.; Lee, J.; Maddison, C.J.; Dahl, G.E. On Empirical Comparisons of Optimizers for Deep Learning. *arXiv* **2019**, arXiv:1910.05446.
82. Goodfellow, I.; Bengio, Y.; Courville, A. *Deep Learning*; MIT Press: Cambridge, MA, USA, 2016.
83. Glorot, X.; Bengio, Y. Understanding the Difficulty of Training Deep Feedforward Neural Networks. In Proceedings of the Thirteenth International Conference on Artificial Intelligence and Statistics, JMLR Workshop and Conference Proceedings, Sardinia, Italy, 13–15 May 2010; pp. 249–256.
84. Torres, J.F.; Hadjout, D.; Sebaa, A.; Martínez-Álvarez, F.; Troncoso, A. Deep Learning for Time Series Forecasting: A Survey. *Big Data* **2021**, *9*, 3–21. [CrossRef] [PubMed]
85. Tian, Y.; Zhang, Y. A Comprehensive Survey on Regularization Strategies in Machine Learning. *Inf. Fusion* **2022**, *80*, 146–166. [CrossRef]
86. He, K.; Zhang, X.; Ren, S.; Sun, J. Deep Residual Learning for Image Recognition. In Proceedings of the IEEE Conference on Computer Vision and pattern Recognition, Las Vegas, NV, USA, 27–30 June 2016; pp. 770–778.

87. Srivastava, N.; Hinton, G.; Krizhevsky, A.; Sutskever, I.; Salakhutdinov, R. Dropout: A Simple Way to Prevent Neural Networks from Overfitting. *J. Mach. Learn. Res.* **2014**, *15*, 1929–1958.
88. Ioffe, S.; Szegedy, C. Batch Normalization: Accelerating Deep Network Training by Reducing Internal Covariate Shift. In Proceedings of the International Conference on Machine Learning, PMLR, Lille, France, 7–9 July 2015; pp. 448–456.